

PAPER

Cite this: *J. Mater. Chem. A*, 2017, 5, 6170

Cation modulating electrocatalyst derived from bimetallic metal–organic frameworks for overall water splitting†

Yang Wang,^{ab} Wenting Wu,^a Yuan Rao,^a Zhongtao Li,^a Noritatsu Tsubaki^{*b} and Mingbo Wu^{*a}

Metal carbides with unique electrical properties and high catalytic efficiency have attracted tremendous interest for applications involving water electrolysis. In this paper the design of a novel cation modulating electrocatalyst $\text{Ni}_3\text{ZnC}_{0.7}$ using homogeneous bimetallic metal–organic frameworks (NiZn-MOFs) as precursor is reported. The synergistic effect between the unique chemical properties and nanostructure endows $\text{Ni}_3\text{ZnC}_{0.7}$ with a remarkable electrocatalytic performance. The balance of Ni(0) and Ni(II) achieved by Zn modulation is beneficial to both the hydrogen evolution reaction and the oxygen evolution reaction under alkaline conditions. The bifunctional catalyst, $\text{Ni}_3\text{ZnC}_{0.7}$, can drive overall water splitting through a symmetrical double electrode at a current density of 10 mA cm^{-2} with only 1.65 mV, and also shows excellent stability without obvious degradation after 24 h of operation, which makes it a promising noble metal free electrocatalyst. This easy preparation method for $\text{Ni}_3\text{ZnC}_{0.7}$ makes it a promising candidate for a practical answer to water splitting. Furthermore, this cation modulating strategy provides an ingenious way to realize the precise control of the catalysts and can be extended to the synthesis of various novel nanomaterials.

Received 20th January 2017
Accepted 28th February 2017

DOI: 10.1039/c7ta00692f

rsc.li/materials-a

Introduction

Hydrogen derived from water splitting has attracted a great amount of attention because of its clean and recyclable properties.¹ The water splitting includes photo- and electro-induced processes, both of which are largely affected by the performance of the catalysts used.^{2–4} Water splitting *via* electrocatalysis uses a hydrogen evolution reaction (HER) and an oxygen evolution reaction (OER) which occur at the cathode and anode, respectively. At present, the practical application of water splitting *via* electrocatalysis has been hampered by the high cost of electrocatalysts, such as platinum (Pt) for HER and ruthenium oxide (RuO_2) for OER, which are both noble metal catalysts. The exploitation of low cost, efficient and stable electrocatalysts is a vital factor for the industrial application of water splitting *via* electrolysis.⁵ Recently, a variety of earth-abundant catalysts have been proposed as alternatives to noble metal catalysts, such as transition metal sulfides,^{6–9} phosphides,^{10–12} carbides,^{13–15}

oxides,^{16–19} and hydroxides.^{20,21} Furthermore, the combination of HER and OER based on the same catalyst and electrolyte plays a key role in the practical utilization of water splitting. However, it is still a challenge to realize overall water splitting based on the bifunctional catalyst because traditional OER catalysts usually work in an alkali solution, which is usually harmful to the HER catalysts. Therefore, the development of a bifunctional catalyst that is capable of driving both HER and OER is attractive, and it can simplify the fabrication procedures and lower the cost of the water electrolyzer.^{22–24}

Rational modulation of the valence state of the active sites is an effective strategy to improve the catalytic performance of catalysts because electron transfer between metals with different valence states can equilibrate adsorption and desorption energies of the intermediates in the electrocatalysis process.^{25,26} For example, Gong *et al.* investigated the synergistic effect between nickel oxide and nickel (Ni) in facilitating HER catalytic activity.²⁷ Jin *et al.* also discovered the existence of a synergistic effect between cobalt (Co) and cobalt oxides (CoO_x), which makes remarkable contributions to the electrocatalytic activity.¹⁷ Weng *et al.* further verified the reinforced electrocatalytic performance from metal/oxide interfaces (Ni/cerium oxide).²⁸ Furthermore, Duan *et al.* developed a novel bifunctional catalyst CoFePO with outstanding overall water splitting activity through an anion and cation modulating strategy.²⁹ Based on the achievements discussed previously, it was believed that the valence state and electronic states of the metal elements in an electrocatalyst

^aState Key Laboratory of Heavy Oil Processing, College of Chemical Engineering, China University of Petroleum, Qingdao 266580, China. E-mail: wumb@upc.edu.cn

^bDepartment of Applied Chemistry, Graduate School of Engineering, University of Toyama, Gofuku 3190, Toyama 930-8555, Japan. E-mail: tsubaki@eng.u-toyama.ac.jp

† Electronic supplementary information (ESI) available: XRD patterns, N_2 adsorption and desorption isotherms, pore size distribution, high-resolution deconvoluted Zn 2p, and N 1s spectrum, TGA–DSC curve, TEM images, SEM images and double layer capacitance (C_{dl}) of prepared materials. See DOI: 10.1039/c7ta00692f

could be modulated, which plays an important role in water electrocatalysis.^{30,31}

However, the catalysts with a unique nanostructure will improve their electrocatalytic activities.^{32–34} The nanoporous structure will increase the diffusion rate of the electrolyte to the active sites.^{35–37} Many types of substrates with nanostructured properties have also been used to increase the conductivity and mass transfer efficiency of the catalysts, such as graphene,^{38–40} nanotubes,^{41,42} and porous carbon and so on.^{17,43} Recently, metal–organic frameworks (MOFs) with a well-organized structure have been proved to be an ideal precursor to produce nanostructured carbon/metal oxides with highly catalytic activity.^{37,44,45} MOFs with flexible organic ligands and a metal center can be converted to nanostructured materials using a pyrolysis strategy.^{46–49} Nanocarbon materials derived from organic ligands coated on the metallic active sites can increase the conductivity and resistance to corrosion of the catalysts.^{50–52} Furthermore, heteroatoms in organic ligands located in the carbon nanostructures can further modify the electronic property of the catalysts.^{53–57}

In this research, a novel electrocatalyst was developed by using a bimetallic MOF as a precursor. The homogeneous bimetallic MOFs guaranteed the successful formation of Ni₃ZnC_{0.7}, which has not been reported to be an electrocatalyst. Although metal zinc (Zn) cannot drive the electrocatalysis because of its fulfilled 3d orbitals, it can modulate the electronic property of the catalysts by hybridization with the active metal sites.^{9,58–61} The structure–performance relationship of this cation modulating electrocatalyst was clarified using X-ray photoelectron spectroscopy (XPS), transmission electron microscopy (TEM), Raman spectroscopy, Brunauer–Emmett–Teller surface area analysis, and X-ray diffraction (XRD) techniques. The greatly increased performance of Ni₃ZnC_{0.7} in water electrolysis verified that the cation modulating strategy is an effective way to enhance the electrocatalytic activity of the catalysts. This valence state modulating strategy can precisely regulate the structure of catalysts at the atomic level.

Experimental section

Materials synthesis

Firstly, the bimetallic MOFs (NiZn-MOFs) were synthesized, with some modification, according to a method reported in the literature.⁶² Typically, nickel(II) nitrate hexahydrate [Ni(NO₃)₂·6H₂O, 3.0 mmol, 0.87 g, Sinopharm Chemical Reagent Co., Ltd.], zinc nitrate hexahydrate [Zn(NO₃)₂·6H₂O, 1.0 mmol, 0.30 g, Sinopharm Chemical Reagent Co., Ltd.] and triethylenediamine (2.0 mmol, 0.22 g, Aladdin Reagent Co., Ltd.) were dissolved in 50 mL of dimethyl formamide (DMF, Xilong Chemicals Co., Ltd.) under vigorous stirring for 30 min. After that, a 10 mL aqueous solution containing 1,4-benzenedicarboxylic acid (0.70 g, 4.2 mmol, Sinopharm Chemical Reagent Co., Ltd.) was added dropwise. The mixture was magnetically stirred for another 2 h before transferring it to an 80 mL Teflon-lined autoclave and it was then kept at 110 °C for 48 h. The green crystalline powders obtained were recovered using centrifugation, followed by washing with DMF and ethanol and

then finally dried at 60 °C in a vacuum oven overnight. The Ni-MOFs were synthesized following similar procedures without adding Zn(NO₃)₂·6H₂O. Then the NiZn-MOFs obtained were pyrolyzed in a quartz tube furnace under a nitrogen (N₂) atmosphere for 2 h with a heating rate of 2 °C min⁻¹ to produce Ni₃ZnC_{0.7}. The catalysts produced at different pyrolysis temperatures (450, 550, and 650 °C) were denoted as Ni₃ZnC_{0.7}-450, Ni₃ZnC_{0.7}-550, and Ni₃ZnC_{0.7}-650, respectively. The catalyst obtained by pyrolyzing Ni-MOFs at 550 °C was denoted as Ni/C-550.

Characterization

The morphologies of the catalyst obtained were characterized using scanning TEM (STEM; JEM-2100F, Jeol). Raman spectra measurements were carried out using a Raman spectrometer (Model 2000, Renishaw, UK). XPS analysis was performed on an X-ray photoelectron spectrometer (250Xi, ESCALAB) with a monochromatic X-ray source (Al K α $h\nu = 1486.6$ eV). The powder XRD patterns of the catalysts were characterized using an X-ray diffractometer (X'Pert PRO, PANalytical) using Cu K α radiation. The specific surface area and pore size distribution of the catalysts were measured using a surface area measurement instrument (ASAP 2020 M, Micromeritics). All the samples were degassed at 300 °C prior to making the measurements. Thermogravimetric analysis (TGA) and differential scanning calorimetry (DSC) curves were measured under N₂ flow from room temperature to 850 °C, with a heating rate of 10 °C min⁻¹, using a simultaneous thermal analyzer (STA 409 PC Luxx, Netzsch-Gerätebau).

Electrochemical testing

The HER and OER performances of Ni₃ZnC_{0.7} were characterized using an electrochemical analyzer (CHI 760E, CHI Instruments, Inc., Shanghai) in a three-electrode system using a silver/silver chloride (Ag/AgCl) electrode as the reference electrode and a graphite rod as the counter electrode in N₂-saturated 1 M potassium hydroxide (KOH) electrolyte. The Ni₃ZnC_{0.7} supported on a glassy carbon electrode (GCE, 4 mm diameter, 0.1256 cm²) as working electrode was prepared as follows: 2 mg of catalyst was dispersed in 1 mL of 4 : 1 (volume ratio) water/ethanol mixed solvent containing 10 μ L of 5 wt% Nafion solutions with ultrasonic mixing for about 30 min. Then 15 μ L of the catalyst ink suspension was loaded onto the polished GCE and dried in air (loading ~ 0.24 mg cm⁻²). The linear sweep voltammetry curves were collected at a scan rate of 5 mV s⁻¹. The electrochemical impedance spectra (EIS) testing was carried out from 100 MHz to 0.1 Hz at an overpotential of 200 mV. The electrochemical active surface area (ECSA) of the sample was used to determine the active surface area of the catalyst. The values of ECSA were linearly proportional to the double-layer capacitances (C_{dl}), which can be determined from the linear slope of its current density *versus* scan rate in a non-faradaic region. Accordingly, a series of cyclic voltammograms (CV) were performed at various scan rates (5, 10, 20, 50, 100 mV s⁻¹) in a non-faradaic region 1.3–1.4 V *versus* a reversible hydrogen electrode (RHE) range to determine the C_{dl} . The long-term

durability test was performed using chronoamperometry measurements. All potentials measured were calibrated to the RHE using the following equation: $E(\text{RHE}) = E(\text{Ag}/\text{AgCl}) + 0.197 \text{ V} + 0.059 \times \text{pH}$. All the data were presented with iR compensation. The overall water splitting performance was conducted using nickel foam (NF) as a working electrode to reach a high catalyst loading (1 mg cm^{-2}). For comparison, the same amount of noble metal catalysts, *i.e.*, platinum/carbon (Pt/C) and RuO_2 were also supported on the NF as cathode and anode, respectively, to drive the overall water splitting process.

Results and discussion

The synthesis procedures of $\text{Ni}_3\text{ZnC}_{0.7}$ are shown in Fig. 1a. Firstly, the homogeneous bimetallic MOFs were synthesized using a hydrothermal method. Catalysts were then prepared by pyrolyzing the corresponding MOF precursor. The XRD patterns of bimetallic MOFs (NiZn-MOF) in Fig. S1 (ESI[†]) exhibit similar strong diffraction peaks as Ni-MOFs because of the similar ionic radius and electronegativity of Ni and Zn, which confirms that they form a homogeneous distribution of bimetallic MOFs rather forming individual phases. The catalyst obtained exhibited a hierarchical pore structure compared to the microporous NiZn-MOFs, which is beneficial for the diffusion of electrolyte during the electrocatalysis process (Fig. S3 and Table S1; ESI[†]). The compositions of the bifunctional catalysts prepared at different carbonization temperatures are shown in Fig. 1b. Zinc oxide (ZnO) was found in the sample synthesized at a low temperature (450°C). The higher pyrolysis temperatures (550°C and 660°C) endow a high carbothermic reduction

ability that guarantees the pure crystalline phase of $\text{Ni}_3\text{ZnC}_{0.7}$. The XRD patterns of $\text{Ni}_3\text{ZnC}_{0.7}$ exhibit a cubic crystalline phase with typical diffraction peaks at around 42.8° , 49.8° , and 73.1° , which are assigned to the 111, 200, and 220 planes of $\text{Ni}_3\text{ZnC}_{0.7}$, respectively (Fig. S1 (ESI[†]) and 1b). It is noted that the typical diffraction peaks of $\text{Ni}_3\text{ZnC}_{0.7}$ exhibit a small shift compared with those of Ni/C, which indicates that Zn atoms are inserted into the crystal lattice of $\text{Ni}_3\text{ZnC}_{0.7}$. In order to clarify the formation mechanism of $\text{Ni}_3\text{ZnC}_{0.7}$, a series of $\text{Ni}_3\text{ZnC}_{0.7}$ with different pyrolysis times and temperatures were prepared. Firstly, the pyrolysis time of bimetallic MOFs was prolonged. As illustrated in Fig. S2 (ESI[†]), $\text{Ni}_3\text{ZnC}_{0.7}$ -550-6 (pyrolyzed at 550°C for 6 h) retains the pure crystalline phase of $\text{Ni}_3\text{ZnC}_{0.7}$. Whereas, $\text{Ni}_3\text{ZnC}_{0.7}$ -650-6 exhibits the typical diffraction peaks of Ni, which verifies the occurrence of sublimation of Zn during the pyrolysis process under higher temperatures. Furthermore, Zn sublimation in $\text{Ni}_3\text{ZnC}_{0.7}$ -750-2 can also be found. It can be concluded that both the pyrolysis time and temperature affect the crystalline structure of $\text{Ni}_3\text{ZnC}_{0.7}$. The aggregation of $\text{Ni}_3\text{ZnC}_{0.7}$ nanoparticles prepared at higher temperatures and prolonged pyrolysis time can be seen in the TEM images (Fig. S7; ESI[†]), which can also be calculated using the Scherrer equation (Table S2; ESI[†]). TGA–DSC analysis was performed in a N_2 atmosphere to clarify the synthetic process of $\text{Ni}_3\text{ZnC}_{0.7}$. As shown in Fig. S4 (ESI[†]), three weight loss steps can be observed in the pyrolysis process. The first weight loss step (a step illustrated in Fig. S4; ESI[†]) can be attributed to the loss of solvent molecules accommodated in the cavities of the MOFs. The second weight loss step (b step) corresponds to the decomposition of the organic host contained in the MOFs.⁶³ The third

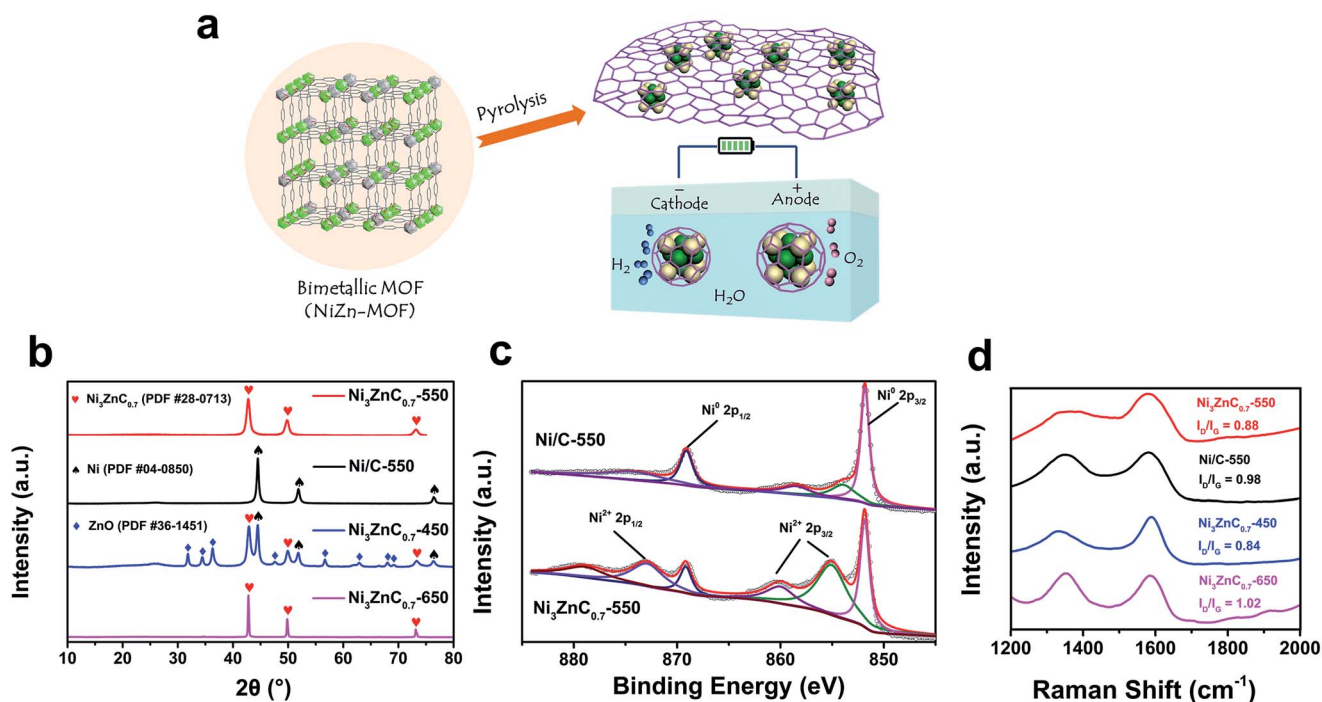


Fig. 1 (a) Scheme of the synthesis procedure of $\text{Ni}_3\text{ZnC}_{0.7}$. (b) XRD patterns of samples prepared at different pyrolysis temperatures. (c) XPS results of Ni 2p spectra of $\text{Ni}_3\text{ZnC}_{0.7}$ -550 and Ni/C-550. (d) Raman spectra of the corresponding catalysts.

weight loss step (c step, around 500–600 °C) can be assigned to the consumption of carbonaceous materials in the ZnO reduction process. During this process, the carbonaceous materials deoxidized ZnO and were then evaporated in the form of carbon dioxide and carbon monoxide.⁶⁴ These three weight loss steps correspond well to the endothermic peaks seen in the DSC curve. This phenomenon also agrees with the variation of crystalline structure of the catalysts obtained at different pyrolysis temperatures (Fig. S2; ESI†). Furthermore, XPS was employed to clarify the surface chemical properties of the catalysts (Fig. 1c and S5; ESI†). As illustrated in Table S1 (ESI†), the atomic ratio of Ni and Zn which is around 3 : 1 corresponds to the chemical formula of $\text{Ni}_3\text{ZnC}_{0.7}$ as determined using XRD characterization. The Ni $2p_{3/2}$ and Ni $2p_{1/2}$ peaks at 851.8 and 869.1 eV were assigned to metallic Ni(0).²⁷ It is worth noting that the peak intensities of Ni $2p_{3/2}$ and Ni $2p_{1/2}$ corresponding to Ni(II) at 855.0, 860.0, and 872.8 eV were enhanced after Zn doping, which means that Zn doping can modulate the valence state of the Ni metal. The balance between Ni(0) and Ni(II) has a synergistic effect on their electrocatalytic performance. It has been verified that the electron transfer between Ni(0) and Ni(II) can promote the catalytic performance of the electrocatalysts.^{17,27,28} The N 1s spectrum of $\text{Ni}_3\text{ZnC}_{0.7}$ can be deconvoluted into pyrrolic, pyridinic, and oxidized N species according to their binding energies (Fig. S5; ESI†).¹⁷ Doped N not only facilitates the electron transfer, but also acts as an active site for the electrocatalysis process.⁵⁷ The carbon structure of the catalysts obtained was also characterized using Raman spectroscopy, as shown in Fig. 1d. The Raman spectra of all the catalysts possess two typical bands at 1350 and 1580 cm^{-1} , which correspond to the disordered carbon and graphitic layers, respectively. Compared with Ni/C-550 ($I_D/I_G = 0.98$), the lower peak intensity ratio of D and G bands for $\text{Ni}_3\text{ZnC}_{0.7}$ -550 ($I_D/I_G = 0.88$) indicates an increase in the average size of sp^2 domains after Zn doping, which can increase the conductivity of the catalyst. Surprisingly, Zn doping plays a vital role not only in modulating the valence state and electronic state of the metal elements, but also in tailoring the chemical properties of the coated carbon layers. The I_D/I_G increases with increasing pyrolysis temperature, which confirms that higher pyrolysis temperatures produce more defects.^{60,65}

$\text{Ni}_3\text{ZnC}_{0.7}$ exhibits a sphere-like morphology as shown in Fig. S6 (ESI†). $\text{Ni}_3\text{ZnC}_{0.7}$ nanoparticles are uniformly dispersed on the carbon carriers as illustrated in Fig. 2a. In the HRTEM image (Fig. 2b), it is obvious that $\text{Ni}_3\text{ZnC}_{0.7}$ nanoparticles are packaged by a few carbon layers, which are beneficial to the prevention of corrosion and aggregation of the nanoparticles during the reaction process. The lattice fringes with a 0.211 nm interspace corresponding to (111) lattice planes of $\text{Ni}_3\text{ZnC}_{0.7}$ can also be identified from the HRTEM images (see inset of Fig. 2b). This unique morphology of $\text{Ni}_3\text{ZnC}_{0.7}$ benefits from the pyrolysis of homogeneous bimetallic-MOFs, which exhibit a periodic unit structure. Fig. 2c shows the STEM image of $\text{Ni}_3\text{ZnC}_{0.7}$. As expected, Ni, Zn, and C are distributed uniformly as illustrated in the corresponding elemental mapping images.

The electrocatalytic performances of catalysts obtained on HER and OER were examined in 1 M aqueous KOH solution

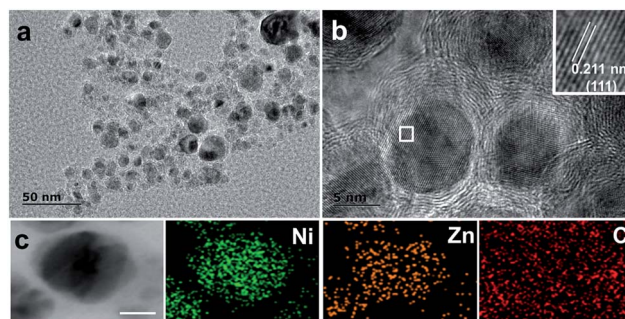


Fig. 2 (a) TEM and (b) High Resolution TEM (HRTEM) images of $\text{Ni}_3\text{ZnC}_{0.7}$, inset is the lattice fringes corresponding to the (111) lattice planes of $\text{Ni}_3\text{ZnC}_{0.7}$. (c) STEM image of $\text{Ni}_3\text{ZnC}_{0.7}$ -550 (scale bar, 100 nm) and the corresponding elemental mapping of Ni, Zn, and C.

using a three-electrode system. From Fig. 3a, it can be seen that $\text{Ni}_3\text{ZnC}_{0.7}$ -550 exhibits excellent HER activity, with a low overpotential of 93 mV to achieve a current density of 10 mA cm^{-2} , which is higher than the 40 mV obtained with the best HER catalyst (Pt/C), but much less than that obtained for other contrast samples. The HER kinetics of $\text{Ni}_3\text{ZnC}_{0.7}$ was clarified using Tafel plots as illustrated in Fig. 3b. The Tafel slope of $\text{Ni}_3\text{ZnC}_{0.7}$ -550 is 48 mV dec^{-1} , which is close to the 36 mV dec^{-1} of Pt/C, suggesting that it follows an electrochemical desorption controlled Volmer–Heyrovsky mechanism.⁶⁶ The higher Tafel slopes of Ni/C-550, $\text{Ni}_3\text{ZnC}_{0.7}$ -450, and $\text{Ni}_3\text{ZnC}_{0.7}$ -650 (94, 120, and 100 mV dec^{-1} , respectively) suggest that HER catalyzed by these catalysts are dominated by the Volmer step, which is a discharge process. The electrochemical impedance spectra (EIS) testing was carried out over the frequency range of 100

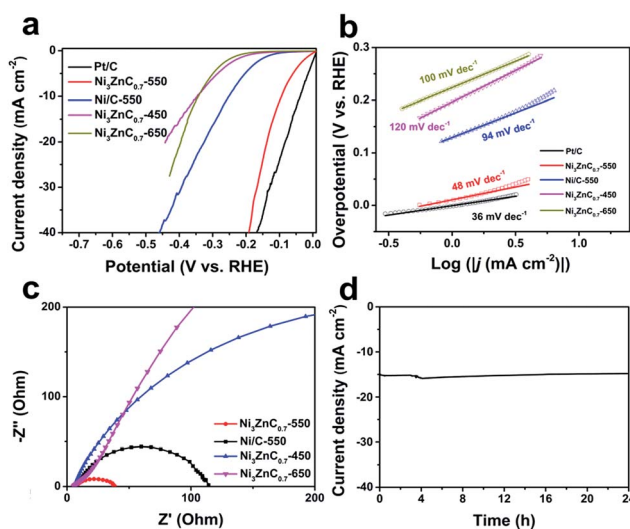


Fig. 3 (a) Polarization curves of Pt/C and samples prepared at different pyrolysis temperatures measured in 1 M KOH with a sweep rate of 5 mV s^{-1} . (b) Tafel plots of the corresponding samples in 1 M KOH. (c) Nyquist plots measured over the frequency range of 100 MHz to 0.1 Hz at an overpotential of 200 mV in 1 M KOH. (d) Time-dependent current density curve of $\text{Ni}_3\text{ZnC}_{0.7}$ -550 at a constant overpotential of 120 mV over 24 h.

MHz to 0.1 Hz at an overpotential of 200 mV to further clarify the relationship between the structure and function of the electrocatalysts (Fig. 3c). The semicircles in the Nyquist plot are attributed to the charge-transfer resistance R_{CT} , and a lower value corresponds to faster charge transfer. $\text{Ni}_3\text{ZnC}_{0.7-550}$ exhibits a smaller R_{CT} (34 Ω) compared with the 109 Ω of Ni/C-550, implying a much faster electron transfer process and higher activity after Zn doping. Furthermore, $\text{Ni}_3\text{ZnC}_{0.7-450}$ and $\text{Ni}_3\text{ZnC}_{0.7-650}$ exhibit a large R_{CT} value because of the impurity crystalline phase and sintering of nanoparticles caused by high pyrolysis temperature, respectively. The smaller charge transfer resistance of $\text{Ni}_3\text{ZnC}_{0.7-550}$ compared with that of $\text{Ni}_3\text{ZnC}_{0.7-650}$ can be attributed to their different structure. $\text{Ni}_3\text{ZnC}_{0.7-550}$ nanoparticles packaged by few carbon layers are anchored on the carbon carriers uniformly (Fig. 2a). This unique structure is beneficial for accelerating the charge transfer process under the electrocatalytic operational conditions. Whereas $\text{Ni}_3\text{ZnC}_{0.7-650}$ discards this special structure because of the sacrifice of carbon carriers at higher pyrolysis temperature. As shown in TEM images (Fig. S7; ESI[†]), the nanoparticles of $\text{Ni}_3\text{ZnC}_{0.7-650}$ have an isolated distribution without conductive carbon layers that will slow down the charge transfer process. The decreasing carbon content of $\text{Ni}_3\text{ZnC}_{0.7-650}$ can also be proved by the XPS results (Table S1; ESI[†]). However, the increasing nanoparticle size of $\text{Ni}_3\text{ZnC}_{0.7-650}$ (Fig. S7 and Table S2; ESI[†]) with fewer exposed active sites is also responsible for the low electrocatalytic activity. This trend of variation of R_{CT} is also consistent with the diverse property of carbon layers characterized by the Raman spectra (Fig. 1d). The electrochemical active surface area (ECSA) of the samples were visualized by calculating the double-layer capacitances (C_{dl}), which were linearly proportional to the ECSA and can be determined from the CVs.⁶⁷ As shown in Fig. S8 (ESI[†]), the higher C_{dl} of $\text{Ni}_3\text{ZnC}_{0.7-550}$ (26.9 mF cm^{-2}) compared with the 12.2 mF cm^{-2} of Ni/C-550 indicates an obvious increase in the amount of active sites after Zn doping, which is consistent with the results obtained from the XPS characterization. The lower C_{dl} of $\text{Ni}_3\text{ZnC}_{0.7-450}$ (4.1 mF cm^{-2}) and $\text{Ni}_3\text{ZnC}_{0.7-650}$ (5.5 mF cm^{-2}) indicate that fewer active sites existed, and this is responsible for their poor electrocatalytic activity. The ECSA of $\text{Ni}_3\text{ZnC}_{0.7-550}$ is more than four times than that of $\text{Ni}_3\text{ZnC}_{0.7-650}$. In order to clarify the structure-

performance relationship of the catalysts, the current density of $\text{Ni}_3\text{ZnC}_{0.7-550}$ and $\text{Ni}_3\text{ZnC}_{0.7-650}$ was normalized using their corresponding relative ECSA (Fig. S9; ESI[†]). The catalytic activity gap between $\text{Ni}_3\text{ZnC}_{0.7-550}$ and $\text{Ni}_3\text{ZnC}_{0.7-650}$ after ECSA normalization is not as obvious as that after the geometric area normalization, highlighting the role of ECSA in enhancing the electrocatalytic performance.⁶⁸ As a key factor that affects its practical application, the HER durability of $\text{Ni}_3\text{ZnC}_{0.7-550}$ was measured at a constant overpotential of 120 mV. As shown in Fig. 3d, the current density exhibits negligible degradation even after 24 h. This excellent stability of $\text{Ni}_3\text{ZnC}_{0.7-550}$ can be ascribed to the unique and protective carbon layers. The HER performance of $\text{Ni}_3\text{ZnC}_{0.7-550}$ can be competitive with other non-noble metal electrocatalysts reported recently (Table S3; ESI[†]).

$\text{Ni}_3\text{ZnC}_{0.7-550}$ also displays high OER activity, which requires an overpotential of 320 mV to achieve 10 mA cm^{-2} of current density, which is comparable to the benchmark OER catalyst RuO_2 ($\eta_{10\text{-OER}} = 308$ mV), as shown in Fig. 4a. Surprisingly, the current density of $\text{Ni}_3\text{ZnC}_{0.7-550}$ is even higher than that of RuO_2 when the overpotential is above 1.56 V, which indicates its excellent OER activity. Additionally, the smaller Tafel slope of $\text{Ni}_3\text{ZnC}_{0.7-550}$ (52 mV dec^{-1}) compared with those of RuO_2 (68 mV dec^{-1}), Ni/C-550 (81 mV dec^{-1}), $\text{Ni}_3\text{ZnC}_{0.7-450}$ (89 mV dec^{-1}), and $\text{Ni}_3\text{ZnC}_{0.7-650}$ (100 mV dec^{-1}) indicates its favorable OER kinetics (Fig. 4b). The low overpotential and small Tafel slope of $\text{Ni}_3\text{ZnC}_{0.7-550}$ are comparable to the non-noble metal electrocatalysts reported recently (Table S4; ESI[†]). In general, $\text{Ni}_3\text{ZnC}_{0.7-550}$ with atomic modulated catalytic interfaces will facilitate not only HER activity but also OER activity. The long-term durability of $\text{Ni}_3\text{ZnC}_{0.7-550}$ for OER was performed using chronoamperometric measurements as shown in Fig. 4c. The constant voltage of 330 mV can drive a stable current density of ~ 15 mA cm^{-2} for 24 h without obvious degradation. After OER stability tests over 24 h, SEM, TEM, XRD, and XPS characterizations were performed to check the morphology and structure changes of $\text{Ni}_3\text{ZnC}_{0.7-550}$. As shown in Fig. S10a and b (ESI[†]), the morphology of $\text{Ni}_3\text{ZnC}_{0.7-550}$ is well maintained after long-term OER tests. Furthermore, the pure crystalline phase of $\text{Ni}_3\text{ZnC}_{0.7-550}$ suggests that there were no significant composition and structure changes after 24 h of OER tests (Fig. S10d;

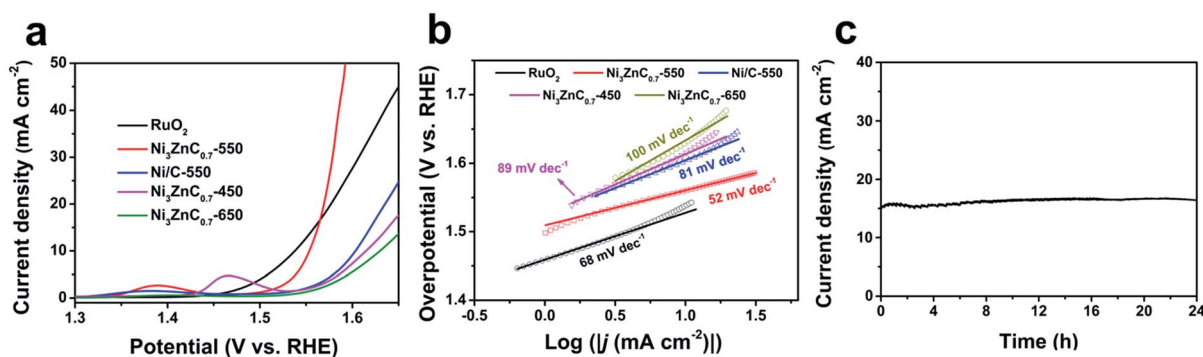


Fig. 4 (a) Polarization curves of RuO_2 and samples prepared at different pyrolysis temperatures measure in 1 M KOH with a sweep rate of 5 mV s^{-1} . (b) Tafel plots of the corresponding samples in 1 M KOH. (c) Time-dependent current density curve of $\text{Ni}_3\text{ZnC}_{0.7-550}$ at a constant overpotential of 330 mV over 24 h.

ESI†). However, the increasing peak intensity of Ni(II) shown in the XPS spectra indicates that the surface of Ni₃ZnCo_{0.7} was partially oxidized (Fig. S10c; ESI†). This phenomenon is consistent with the previously reported results that metal oxide or hydroxide formed on the surface of the catalysts can act as active site for OER, but they are hard to detect using XRD spectra.^{23,69}

The overall water splitting activity was measured in a two-electrode system made by the authors with Ni₃ZnCo_{0.7}-550 supported on a Ni foam as electrode in 1 M KOH solution. For comparison, the same amount of remarkable HER catalyst (Pt/C) and OER catalyst (RuO₂) were also supported on Ni foam as cathode and anode, respectively. As shown in Fig. 5a, Ni₃ZnCo_{0.7}-550 requires an overpotential of 1.65 V to obtain a current density of 10 mA cm⁻², which is very close to the 1.63 V of the state-of-the-art Pt/C–RuO₂ counterparts and much higher than the 1.90 V of Ni foam. The long-term stability of Ni₃ZnCo_{0.7}-550 for overall water splitting was tested using a fixed voltage (1.70 V) as illustrated in Fig. 5b. A constant 20 mA cm⁻² of current density can be well maintained without obvious deactivation after 24 h, which represents the excellent durability of Ni₃ZnCo_{0.7}-550 as a bifunctional catalyst for overall water splitting. Furthermore, an AAA battery with a nominal voltage of 1.5 V can drive overall water splitting with Ni₃ZnCo_{0.7}-550 as a bifunctional catalyst. The obvious gas bubbles released from the electrodes as shown in Fig. 5c confirm the high efficiency of Ni₃ZnCo_{0.7}-550. The mechanical stability of Ni₃ZnCo_{0.7} as catalyst should be considered. From the photography of the electrolyte after overall water splitting for 24 h, no obvious catalysts were lost from the electrode (Fig. S11; ESI†). The hierarchical pore

structure and uniform dispersed active sites of Ni₃ZnCo_{0.7}-550 guarantee the H₂ and O₂ produced at cathode and anode were released from the electrode homogeneously instead of breaking the catalyst layer coated on the electrode.

Conclusion

In summary, a novel and efficient bifunctional catalyst has been developed for overall water splitting using the thermal annealing of bimetallic MOFs. The as-made Ni₃ZnCo_{0.7} catalyst exhibits remarkable HER and OER performance with low overpotential and long-term stability. Furthermore, Ni₃ZnCo_{0.7} can execute overall water splitting at 10 mA cm⁻² with only 1.65 V, which is close to the 1.63 V of the state-of-the-art Pt/C–RuO₂. This excellent electrocatalytic activity of Ni₃ZnCo_{0.7} can be assigned to the synergistic effect of the cation modulating strategy and the unique nanostructured Ni₃ZnCo_{0.7} derived from the MOFs precursor. The excellent electrocatalytic performance of Ni₃ZnCo_{0.7} confirms that the atomic modulating strategy is an effective way to realize the optimization of catalytic activity. This will enrich the horizon of the design and synthesis of the electrocatalyst.

Acknowledgements

This work is supported by the National Natural Science Foundation of China (No. 51572296, U1662113, 51372277) and the Fundamental Research Funds for the Central Universities (No. 15CX08005A).

Notes and references

- 1 J. A. Turner, *Science*, 2004, **305**, 972–974.
- 2 Q. Liang, Z. Li, X. Yu, Z. H. Huang, F. Kang and Q. H. Yang, *Adv. Mater.*, 2015, **27**, 4634–4639.
- 3 J. F. Callejas, J. M. McEnaney, C. G. Read, J. C. Crompton, A. J. Bicch, E. J. Popczun, T. R. Gordon, N. S. Lewis and R. E. Schaak, *ACS Nano*, 2014, **8**, 11101–11107.
- 4 B. Weng, W. Wei, Yiliguma, H. Wu, A. M. Alenizi and G. Zheng, *J. Mater. Chem. A*, 2016, **4**, 15353–15360.
- 5 X. Zou and Y. Zhang, *Chem. Soc. Rev.*, 2015, **44**, 5148–5180.
- 6 Z. F. Huang, J. Song, K. Li, M. Tahir, Y. T. Wang, L. Pan, L. Wang, X. Zhang and J. J. Zou, *J. Am. Chem. Soc.*, 2016, **138**, 1359–1365.
- 7 X. Geng, W. Sun, W. Wu, B. Chen, A. Al-Hilo, M. Benamara, H. Zhu, F. Watanabe, J. Cui and T.-P. Chen, *Nat. Commun.*, 2016, **7**, 10672.
- 8 Y. Li, H. Wang, L. Xie, Y. Liang, G. Hong and H. Dai, *J. Am. Chem. Soc.*, 2011, **133**, 7296–7299.
- 9 H. Zhu, J. Zhang, R. Yanzhang, M. Du, Q. Wang, G. Gao, J. Wu, G. Wu, M. Zhang, B. Liu, J. Yao and X. Zhang, *Adv. Mater.*, 2015, **27**, 4752–4759.
- 10 E. J. Popczun, J. R. McKone, C. G. Read, A. J. Bicch, A. M. Wiltrout, N. S. Lewis and R. E. Schaak, *J. Am. Chem. Soc.*, 2013, **135**, 9267–9270.

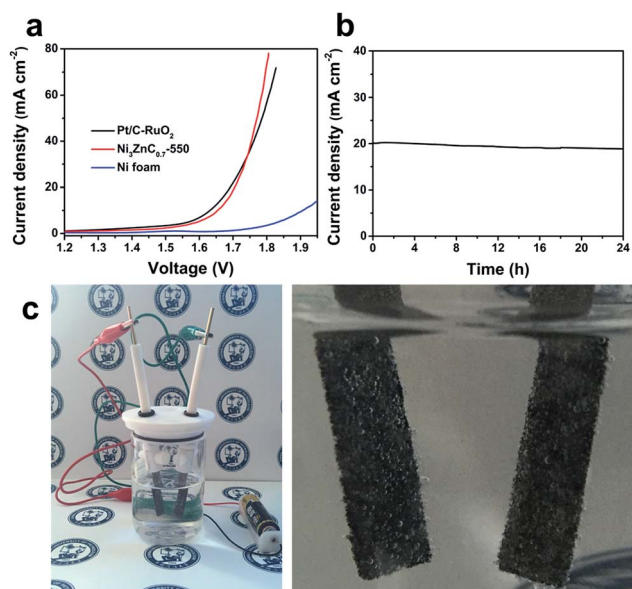


Fig. 5 (a) Polarization curves of Pt/C–RuO₂, Ni₃ZnCo_{0.7}-550, and Ni foam tested by a self-made two-electrode system in 1 M KOH. (b) Time-dependent current density curve of Ni₃ZnCo_{0.7}-550 as a bifunctional catalyst for the overall water splitting. (c) Photography of Ni₃ZnCo_{0.7}-550 catalyzed overall water splitting powered by an AAA battery with a nominal voltage of 1.5 V.

- 11 M. Ledendecker, S. Krickalderön, C. Papp, H. P. Steinrück, M. Antonietti and M. Shalom, *Angew. Chem., Int. Ed.*, 2015, **54**, 12361–12365.
- 12 L. Jiao, Y. X. Zhou and H. L. Jiang, *Chem. Sci.*, 2016, **7**, 1690–1695.
- 13 M. R. Lukatskaya, Y. Gogotsi, T. F. Jaramillo and A. Vojvodic, *ACS Energy Lett.*, 2016, **1**, 589–594.
- 14 R. Ma, Y. Zhou, Y. Chen, P. Li, Q. Liu and J. Wang, *Angew. Chem., Int. Ed.*, 2015, **54**, 14723–14727.
- 15 Y. Liu, G. Yu, G. D. Li, Y. Sun, T. Asefa, W. Chen and X. Zou, *Angew. Chem., Int. Ed.*, 2015, **54**, 10752–10757.
- 16 X. Gao, H. Zhang, Q. Li, X. Yu, Z. Hong, X. Zhang, C. Liang and Z. Lin, *Angew. Chem., Int. Ed.*, 2016, **55**, 6290–6294.
- 17 H. Jin, J. Wang, D. Su, Z. Wei, Z. Pang and Y. Wang, *J. Am. Chem. Soc.*, 2015, **137**, 2688–2694.
- 18 R. Wu, J. Zhang, Y. Shi, D. Liu and B. Zhang, *J. Am. Chem. Soc.*, 2015, **137**, 6983–6986.
- 19 J. Li, Y. Wang, T. Zhou, H. Zhang, X. Sun, J. Tang, L. Zhang, A. M. Al-Enizi, Z. Yang and G. Zheng, *J. Am. Chem. Soc.*, 2015, **137**, 14305–14312.
- 20 C. Tang, H. Wang, H. Wang, Q. Zhang, G. Tian, J. Nie and F. Wei, *Adv. Mater.*, 2015, **27**, 4516–4522.
- 21 X. Lu and C. Zhao, *Nat. Commun.*, 2015, **6**, 6616.
- 22 X. Jia, Y. Zhao, G. Chen, L. Shang, R. Shi, X. Kang, G. I. N. Waterhouse, L. Z. Wu, C. H. Tung and T. Zhang, *Adv. Energy Mater.*, 2016, **6**, 1502585.
- 23 X. Zhang, H. Xu, X. Li, Y. Li, T. Yang and Y. Liang, *ACS Catal.*, 2016, **6**, 580–588.
- 24 J. Wang, H. X. Zhong, Z. L. Wang, F. L. Meng and X. B. Zhang, *ACS Nano*, 2016, **10**, 2342–2348.
- 25 V. R. Stamenkovic, D. Strmcnik, P. P. Lopes and N. M. Markovic, *Nat. Mater.*, 2017, **16**, 57–69.
- 26 B. Weng, F. Xu, C. Wang, W. Meng, C. R. Grice and Y. Yan, *Energy Environ. Sci.*, 2017, **10**, 121–128.
- 27 M. Gong, W. Zhou, M. C. Tsai, J. Zhou, M. Guan, M. C. Lin, B. Zhang, Y. Hu, D. Y. Wang, J. Yang, S. J. Pennycook, B. J. Hwang and H. Dai, *Nat. Commun.*, 2014, **5**, 4695.
- 28 Z. Weng, W. Liu, L. C. Yin, R. Fang, M. Li, E. I. Altman, Q. Fan, F. Li, H. M. Cheng and H. Wang, *Nano Lett.*, 2015, **15**, 7704–7710.
- 29 J. Duan, S. Chen, A. Vasileff and S. Z. Qiao, *ACS Nano*, 2016, **10**, 8738–8745.
- 30 B. Zhang, C. Xiao, S. Xie, J. Liang, X. Chen, Y. Tang, B. Zhang, C. Xiao, S. Xie, J. Liang, X. Chen and Y. Tang, *Chem. Mater.*, 2016, **28**, 6934–6941.
- 31 K. Fominykh, P. Chernev, I. Zaharieva, J. Sicklinger, G. Stefanic, M. Döblinger, A. Müller, A. Pokharel, S. Böcklein, C. Scheu, T. Bein and D. Fattakhova-Rohlfing, *ACS Nano*, 2015, **9**, 5180–5188.
- 32 X. W. Lou, L. A. Archer and Z. Yang, *Adv. Mater.*, 2008, **20**, 3987–4019.
- 33 A. Mahmood, W. Guo, H. Tabassum and R. Zou, *Adv. Energy Mater.*, 2016, **6**, 1600423.
- 34 G. Tian, M. Zhao, D. Yu, X. Kong, J. Huang, Q. Zhang and F. Wei, *Small*, 2014, **10**, 2251–2259.
- 35 C. R. Pérez, S. Yeon, J. Ségalini, V. Presser, P. Taberna, P. Simon and Y. Gogotsi, *Adv. Funct. Mater.*, 2013, **23**, 1081–1089.
- 36 X. Y. Yu, Y. Feng, Y. Jeon, B. Guan, X. W. Lou and U. Paik, *Adv. Mater.*, 2016, **28**, 9006–9011.
- 37 H. Hu, B. Guan, B. Xia and X. W. Lou, *J. Am. Chem. Soc.*, 2015, **137**, 5590–5595.
- 38 C. T. Zhao, C. Yu, S. H. Liu, J. Yang, X. M. Fan, H. W. Huang and J. Qiu, *Adv. Funct. Mater.*, 2015, **25**, 6913–6920.
- 39 X. Meng, C. Yu, X. Song, Y. Liu, S. Liang, Z. Liu, C. Hao and J. Qiu, *Adv. Energy Mater.*, 2015, **5**, 1500180.
- 40 H. Yan, C. Tian, L. Wang, A. Wu, M. Meng, L. Zhao and H. Fu, *Angew. Chem., Int. Ed.*, 2015, **54**, 6325–6329.
- 41 T. Wang, Y. Guo, Z. Zhou, X. Chang, J. Zheng and X. Li, *ACS Nano*, 2016, **10**, 10397–10403.
- 42 Q. Liu, J. Tian, W. Cui, P. Jiang, N. Cheng, A. M. Asiri and X. Sun, *Angew. Chem., Int. Ed.*, 2014, **53**, 6710–6714.
- 43 B. You, N. Jiang, M. Sheng, S. Gul, J. Yano and Y. Sun, *Chem. Mater.*, 2015, **27**, 7636–7642.
- 44 B. Y. Guan, L. Yu and X. W. Lou, *Energy Environ. Sci.*, 2016, **9**, 3092–3096.
- 45 X. Y. Yu, L. Yu, H. Bin Wu and X. W. Lou, *Angew. Chem., Int. Ed.*, 2015, **54**, 5331–5335.
- 46 P. Pachfule, D. Shinde, M. Majumder and Q. Xu, *Nat. Chem.*, 2016, **8**, 718–724.
- 47 H. B. Wu, B. Y. Xia, L. Yu, X. Y. Yu and X. W. Lou, *Nat. Commun.*, 2015, **6**, 6512.
- 48 B. Liu, H. Shioyama, T. Akita and Q. Xu, *J. Am. Chem. Soc.*, 2008, **130**, 5390–5391.
- 49 S. Niu, Z. Wang, T. Zhou, M. Yu, M. Yu and J. Qiu, *Adv. Funct. Mater.*, 2017, **27**, 1605332.
- 50 Y. Z. Chen, C. Wang, Z. Y. Wu, Y. Xiong, Q. Xu, S. H. Yu and H. L. Jiang, *Adv. Mater.*, 2015, **27**, 5010–5016.
- 51 H. Zhang, Z. Ma, J. Duan, H. Liu, G. Liu, T. Wang, K. Chang, M. Li, L. Shi, X. Meng, K. Wu and J. Ye, *ACS Nano*, 2016, **10**, 684–694.
- 52 Y. Yang, Z. Lun, G. Xia, F. Zheng, M. He and Q. Chen, *Energy Environ. Sci.*, 2015, **8**, 3563–3571.
- 53 G. Tian, Q. Zhang, B. Zhang, Y. Jin, J. Huang, D. S. Su and F. Wei, *Adv. Funct. Mater.*, 2014, **24**, 5956–5961.
- 54 S. Liu, Y. Dong, C. Zhao, Z. Zhao, C. Yu, Z. Wang and J. Qiu, *Nano Energy*, 2015, **12**, 578–587.
- 55 J. Liang, Y. Jiao, M. Jaroniec and S. Z. Qiao, *Angew. Chem., Int. Ed.*, 2012, **51**, 11496–11500.
- 56 J. Zhang, Z. Zhao, Z. Xia and L. Dai, *Nat. Nanotechnol.*, 2015, **10**, 444–452.
- 57 Y. Zheng, Y. Jiao, Y. Zhu, L. H. Li, Y. Han, Y. Chen, A. Du, M. Jaroniec and S. Z. Qiao, *Nat. Commun.*, 2014, **5**, 3783.
- 58 X. Zou, A. Goswami and T. Asefa, *J. Am. Chem. Soc.*, 2013, **135**, 17242–17245.
- 59 Q. Dong, Q. Wang, Z. Dai, H. Qiu and X. Dong, *ACS Appl. Mater. Interfaces*, 2016, **8**, 26902–26907.
- 60 J. Su, G. Xia, R. Li, Y. Yang, J. Chen, R. Shi, P. Jiang and Q. Chen, *J. Mater. Chem. A*, 2016, **4**, 9204–9212.
- 61 X. Liu, Z. Chang, L. Luo, T. Xu, T. Lei, J. Liu and X. Sun, *Chem. Mater.*, 2014, **26**, 1889–1895.

- 62 D. N. Dybtsev, H. Chun and K. Kim, *Angew. Chem., Int. Ed.*, 2004, **43**, 5033–5036.
- 63 H. L. Jiang, B. Liu, Y. Q. Lan, K. Kuratani, T. Akita, H. Shioyama, F. Q. Zong and Q. Xu, *J. Am. Chem. Soc.*, 2011, **133**, 11854–11857.
- 64 S. J. Yang, T. Kim, J. H. Im, Y. S. Kim, K. Lee, H. Jung and C. R. Park, *Chem. Mater.*, 2012, **24**, 464–470.
- 65 F. Zheng, Y. Yang and Q. Chen, *Nat. Commun.*, 2014, **5**, 5261.
- 66 Y. Shi and B. Zhang, *Chem. Soc. Rev.*, 2016, **45**, 1529–1541.
- 67 Y. Jiao, Y. Zheng, M. Jaroniec and S. Z. Qiao, *Chem. Soc. Rev.*, 2015, **44**, 2060–2086.
- 68 J. F. Zhang, Y. C. Hu, D. L. Liu, Y. Yu and B. Zhang, *Adv. Sci.*, 2016, 1600343.
- 69 Y. Xu, W. G. Tu, B. Z. Zhang, S. M. Yin, Y. Z. Huang, M. Kraft and R. Xu, *Adv. Mater.*, 2017, DOI: 10.1002/adma.201605957.